Solution-processed low-bandgap CuIn(S,Se)$_2$ absorbers for high efficiency single junction and monolithic chalcopyrite-perovskite tandem solar cells

Alexander R. Uhl*, Adharsh Rajagopal, James A. Clark, Anna Murray, Thomas Feurer, Stephan Buecheler, Alex K.-Y. Jen, Hugh W. Hillhouse*

Dr. A.R. Uhl, J.A. Clark, A. Murray, Prof. H.W. Hillhouse
Department of Chemical Engineering, Molecular Engineering and Sciences Institute, University of Washington, Seattle, Washington 98195-1652, United States
E-mail: auhl@uw.edu, h2@uw.edu
A. Rajagopal, Prof. A. K.-Y. Jen
Department of Materials Science and Engineering, University of Washington, Seattle, Washington 98195-2120, United States
Prof. A. K.-Y. Jen
Department of Materials Science & Engineering, Department of Chemistry, City University of Hong Kong, Kowloon 999077, Hong Kong
T. Feurer, Dr. S. Buecheler
Laboratory for Thin Films and Photovoltaics, Empa – Swiss Federal Laboratories for Materials Science and Technology, 8600, Dübendorf, Switzerland

A novel molecular-ink deposition route based on thiourea and N,N-dimethylformamide (DMF) is presented that resulted in a certified solar cell efficiency world record for non-vacuum deposited CuIn(S,Se)$_2$ (CIS) absorbers and non-vacuum deposited absorbers with a bandgap of 1.0 eV. We found that by substituting the widely employed solvent dimethyl sulfoxide (DMSO) with DMF, the coordination chemistry of InCl$_3$ could be altered, dramatically improving ink stability, enabling up to 10-fold increased concentrations, omitting the necessity for elevated ink temperatures, and radically accelerating the deposition process. Furthermore, we show that by introducing compositionally-graded precursor films, film porosity, compositional gradients, and the surface roughness of our absorbers are effectively reduced and device conversion efficiencies are increased up to 13.8% (13.1%

certified, active area). The reduced roughness was also seen crucial to realize monolithically interconnected CIS-perovskite tandem devices, where semitransparent $MAPbI_3$ devices are directly deposited on the CIS bottom cell. Proofing the feasibility of this approach, we present monolithic devices with near perfect voltage addition between subcells of up to 1.40 V.

The reduction of greenhouse gas emissions to mitigate climate change while meeting the growing global energy demand is one of the greatest challenges of our time. Renewable energy technologies, such as photovoltaics (PV), have been identified by the Intergovernmental Panel on Climate Change (IPCC) to play a leading role in the necessary transition away from fossil-combustion-based energy sources.[1] To guarantee a wide-spread implementation of PV technology, however, cost-competitiveness to conventional energy sources has to be achieved.

Employing ink-based deposition methods to fabricate PV functional layers has the potential to bring down costs and allow sustainable growth of the technology due to their low capital expenditure, high material utilization, and high throughput, if high device efficiencies and benign reaction mechanisms can be obtained at the same time. Thin film solar cells based on chalcogenide and perovskite absorbers are particularly promising as they have achieved the highest power conversion efficiencies among thin film solar cells of over 22% – exceeding market-leading polycrystalline silicon (pc-Si) – and can be fabricated by liquid deposition methods due to their high absorption constants.[2-5] Moreover, both technologies exhibit a wide range of bandgap tunability, which allows for their integration in solution-processed

tandem solar cells that can further boost device efficiencies by over 40% and promote the reduction of solar electricity prices to values below those of coal or gas.[6]

Tandem solar cells represent an exciting means to increase the power conversion efficiency (PCE) of solar cells by increasing the absorption of photons and reducing thermalization losses of electrons. To date, highest tandem efficiencies up to 38.8% under one sun, however, are based on III-V semiconductors which restricts the use of tandem devices to special markets due to the need for costly epitaxial growth and small area of devices.[7] The recent sprint in hybrid perovskite device efficiency from 3.8% in 2009 to 22% in 2016 has resulted in a tremendous increase in research efforts in perovskite-based tandem devices.[3, 8] Their large bandgaps, low sub-bandgap absorption, and low processing temperatures make perovskite solar cells (PSC) an excellent choice as top cells in tandem devices.[9] Perovskite top cells have been successfully combined with silicon, $Cu(In,Ga)(S,Se)_2$ (CIGS), and perovskite bottom cells achieving device efficiencies up to 26.4%, 23.9%, and 23.1%, respectively.[10] While these results are impressive, the devices typically employ a mechanically-stacked architecture which eases manufacturing but may not be economically preferred due to added costs and absorption and resistive losses from additional substrates and transparent conductive oxides. Moreover, highest PCE hybrid perovskite (HP)-based tandem devices employ heterojunction technology (HJT) or passivated emitter and rear cell (PERC) Si solar cells, which rely on costly lithographic methods and single crystalline absorbers. The combination of PSCs with existing commercial PV technologies, such as pc-Si or CIGS solar modules, in a tandem device could pose the biggest impact for the HP technology and ultimately facilitate the commercialization of PSCs. Due to their thin film nature, CIGS devices offer several advantages compared to c-Si in respect of their use as

bottom cells such as the choice of rigid or flexible substrates, monolithic integration, and solution-processing.[4, 5, 11, 12] Moreover, the bandgap of CIGS can be tuned to values as low as 1.0 eV which is predicted to afford excellent current matching in monolithic tandem devices with the current highest efficiency PSCs with a bandgap of 1.6 eV.[3, 13] Notably, larger bandgap perovskite compositions of 1.7 eV and 1.8 eV, which are required for current-matching in a monolithic configuration with Si (1.1 eV) or low-bandgap perovskite (1.2 eV) bottom cells, respectively, are vulnerable to phase segregation under excess carrier concentration – as caused under illumination – and might thus pose constraints on tandem device performance and stability.[14]

Despite its excellent suitability, however, only a few research teams have reported monolithic tandem devices with CIGS bottom cells to date. Todorov et al. presented up to 10.9% efficient monolithic CIGS-HP tandems employing a thin layer of Ca as top electrode and indium tin oxide (ITO) as recombination layer. Low-bandgap CIGS absorbers (i.e. 1.04 eV) for the 11.4% efficient bottom cells were thereby obtained from hydrazine solutions, whose high toxicity and flammability may pose hindrances for commercialization.[15] Jang et al. reported on up to 11.0% efficient monolithic tandems utilizing electrodeposited 10.6% efficient CuInSe$_2$ devices as bottom cells.[16]

We previously projected current-matched, two-terminal CIS-HP tandem PCEs up to 18.5% by stacking a 13.6% efficient semitransparent MAPbI$_3$ PSC on top of solution-processed 13.0% efficient CuIn(S,Se)$_2$ (CIS) device (Egap = 0.99 eV).[17] Omitting the use of highly toxic and explosive solvents and gases, a molecular-ink process based on dimethyl sulfoxide (DMSO) solvent and thiourea (TU) was thereby employed which resulted in in up to 14.7% efficient CIGS solar cells. Notably, low bandgap CIS devices from that process exhibited up to 13.0% PCE, representing the world record for solution-processed CIS or solution-

processed 1.0 eV bandgap solar cell to date. The formation of copper-TU-chloride complexes and indium-DMSO-chloride complexes was found critical to control oxidation states and loss of metals during processing and to tailor the final composition of the absorber. Despite the benefits of the employed ink chemistry, the low solubility of the $In(DMSO)_3Cl_3$ complex ultimately limited indium concentrations in the ink to 0.1 M or 0.45 M at room temperature or 120°C, respectively. This resulted in the need to heat inks during deposition, the use of numerous deposition cycles to achieve necessary absorber thicknesses, as well as the risk of In loss via filtration of the inks.

Previously, we reported that N,N-dimethylformamide (DMF) could be used as an aprotic solvent to stabilize high valence metal cations Sn(IV) and Ge(IV) in inks at high concentrations for high PCE solution processed $Cu_2ZnSn(S,Se)_4$ and $Cu_2Zn(Ge,Sn)(S,Se)_4$ PV devices.[18] More recently, a 50/50 mix of DMF and isopropanol (IPA) was explored for In(III) stabilization to form CIS, resulting in 3.4% PCE devices with sulfur-rich composition and a bandgap of 1.37 eV.[19] Here, we use DMF only as the solvent and stabilizing ligand for $InCl_3$ enabling a more than 10-fold increase in ink concentration (compared to DMSO). This reduces the number of required spin-coating cycles to build-up an optically thick layer (for the NIR region of the spectrum). We further present a novel compositional stacking sequence (Cu-rich deposition followed by Cu-poor) to tailor the absorber morphology, roughness, and copper composition gradient. By employing the above-mentioned adjustments to our molecular ink route, we could increase the performance for devices with solution-processed CIS absorbers to an improved world record PCE of 13.8% (13.1% certified, active area). Highlighting the improved morphology and roughness of our CIS devices and excellent suitability of low bandgap CIS and $MAPbI_3$ absorbers, we manufactured solution-processed

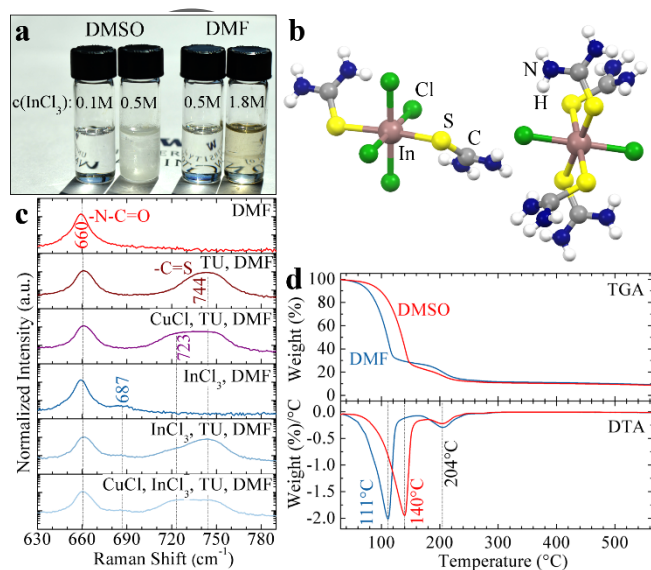monolithic tandem devices with semitransparent hybrid perovskite top cells with efficiencies up to 8.55%.

Figure 1: (a) Photograph of DMSO and DMF molecular inks. DMSO inks precipitate at 0.5 M $InCl_3$ concentration, while DMF inks are stable to concentrations of 1.8 M and higher. (b) Upon addition of IPA to the DMF ink, a neutral indium-thiourea complex $[In(TU)_4Cl_2]^+[In(TU)_2Cl_4]^-$ precipitates (see Table S1 for crystal data). (c) Raman scattering spectra of liquid inks indicate coordination of Cu with TU and In with TU and DMF. (d) Thermogravimetric analysis of DMF and DMSO inks showing clean decomposition of organic species below 250°C.

Molecular-ink precursor solutions were prepared by adding TU, CuCl, and $InCl_3$ to either DMSO or DMF solvent in a ratio TU/Me = 3 and Cu/In = 0.80 if not specified differently. The regents were added in the sequence mentioned and stirred until complete dissolution before adding the next reagent. This dissolution sequence ensures the formation of a stable $Cu(TU)_xCl$ complex which facilitates solvation of CuCl and stabilization of Cu in oxidation state +I, omitting the need for redox reactions throughout the consecutive processing steps in order to form the desired I-III-VI$_2$ absorber compound.[17] **Figure 1a** shows precursor inks with DMSO or DMF solvent and various $InCl_3$ concentrations at room temperature (see also Fig S1). Stable solutions could be obtained for DMSO solvent up to 0.1 M concentration while higher concentrations resulted in cloudy inks due to the precipitation of

In(DMSO)$_3$Cl$_3$.[17] In contrast, precursor solutions employing DMF solvent can facilitate much higher concentrations, as seen for the clear inks with InCl$_3$ concentration of 0.5 M and 1.8 M. The latter was initially heated overnight on a hotplate at 120°C to facilitate dissolution but was then seen to be stable for weeks without additional heating.

In order to examine the coordination of species in the DMF-TU molecular ink route, crystals were isolated for X-ray diffraction (XRD) characterization. We used an anti-solvent approach to facilitate crystal precipitation as both heating of the ink under mild vacuum and ice cooling failed to produce crystals (yielding only an amorphous precipitate). Small amounts of IPA were gradually added to our DMF precursor ink (containing CuCl, InCl$_3$, and TU) until small white crystals precipitated. Crystals were isolated and analyzed with single crystal XRD. **Figure 1b** depicts the unit cell of the complex that comprised both [In(TU)$_4$Cl$_2$]$^+$ and [In(TU)$_2$Cl$_4$]$^-$ species to form a charge neutral complex with overall stoichiometry of 1 In : 3 TU : 3 Cl, which is in agreement to previous reports.[20, 21] These crystals do not prove the presence of TU coordination to In in DMF solution, but suggests the complex may form upon drying. In order to further investigate the coordination in the DMF ink, we performed Raman spectroscopy on liquid inks with various DMF and DMF/TU solutions (see **Figure 1c**). The vibrational N-C=O bending mode of DMF and C=S stretching mode of TU is observed at 660 cm^{-1} and 745 cm^{-1}, respectively, which is in good agreement with literature values.[22, 23] In agreement our previous report, the C=S mode of TU is seen to move to lower wavenumbers (i.e. 723 cm^{-1}) upon addition of CuCl while leaving the DMF bending mode unaffected, indicating the formation of a Cu(TU)$_x$Cl complex. DMF is a strong Lewis base with a partial negative charge on the oxygen that easily coordinates with metal cations. A myriad of complexes have been reported for DMF with bivalent, trivalent, and quadrivalent cations, e.g. Ni(II), Zn(II), Cu(II), Al (III), Ga (III), In (III), Fe (III), or Ti(IV), while no

reports of complexes with monovalent cations were described.[23, 24] Congruently, we also observed that CuCl is not soluble in DMF alone while DMF was able to solubilize InCl$_3$. Accordingly, we found the N-C=O bending mode shifted to higher wavenumbers (687 cm^{-1}) with addition of InCl$_3$. Interestingly, the Raman peak centered at 744 cm^{-1}, corresponding to the C=S stretching mode of TU, is also affected by the addition of InCl$_3$ to a DMF/TU solution. This is seen as an increase in intensity near 723 cm^{-1} similar in character to the changes observed with CuCl addition, but not as significant. This suggests that that both DMF and TU may compete in the first coordination shell of InCl$_3$. The combination of TU and DMF ligands facilitate a much higher solubility of InCl$_3$ than DMSO and TU ligands, enabling the fabrication of higher concentrated precursor inks. Notably, we found that in contrast to DMSO, highly concentrated DMF-based inks (e.g. c(InCl$_3$) = 1.8 M, see Fig. 1a) result in only an increased viscosity rather than precipitation.

The lower molar mass and strength of intermolecular forces between solvent molecules of DMF are also reflected in the lower boiling point of DMF as compared to DMSO (i.e.153 °C and 189 °C for DMF and DMSO, respectively).[25] **Figure 1d** compares the weight loss of precursor inks with both DMF and DMSO solvent in inert atmosphere. Both inks follow a two-step weight loss with the first loss observed at 111 °C and 140 °C, corresponding to the evaporation of DMF and DMSO, respectively, and the second loss for both solvents occurring at 204 °C, consistent with the decomposition of TU.[21, 26] No significant weight loss is apparent beyond 250 °C. However, polymerized or amorphous carbon-nitrogen species (decomposition products from TU) may form at higher temperatures in inert atmospheres and become trapped in the film as growing absorber grains form a diffusion barrier during high temperature anneal in selenium atmosphere (selenization).[27] To avoid this polymerization and trapping of carbon, precursor films were annealed at low temperature

in nitrogen (250 °C) on a hot plate and brought to high temperature during selenization whereupon carbon and nitrogen are removed. To estimate the amount of residual carbon in CISe absorbers after selenization from our DMF molecular ink route and compare the residual carbon content to vacuum-deposited CIS (co-evaporation from elemental sources), glow discharge optical emission spectroscopy (GD-OES) depth profiles were collected from absorber layers from both routes that resulted in >13% PCE devices (see Figure S2 & S3, Table S2).[28] Notably, the detected carbon in both cases is locally confined to the area of the Mo back contact, suggesting the carbon-free nature of the absorbers and a main carbon inclusion pathway through ambient exposure between Mo and absorber deposition.

Co-evaporated CIS absorbers typically employ a Cu-rich growth phase during deposition to improve grain growth, morphology, and device performance by utilizing the occurrence of a liquid Cu-Se phase as fluxing agent.[29] Mimicking the latter, we investigated the use of compositionally-graded precursor layers as a means to facilitate Cu-rich growth conditions while maintaining the overall stoichiometry.[30] As depicted in **Figure 2a**, repeated spin-coating and annealing cycles of compositionally-varied inks were used to fabricate Cu-graded precursors with a Cu-rich bottom layer (i.e. Cu/In=0.85) and Cu-poor top layer (i.e. Cu/In=0.75) in comparison to our standard process with a uniform stoichiometry (i.e. Cu/In=0.80). Precursor films were then selenized with elemental Se vapor in a tubular quartz furnace under equal conditions to obtain $CuIn(S,Se)_2$ absorber films. Profilometry measurements of the absorber surface reveals a significant reduction of the root-mean-square (RMS) roughness for the Cu-graded approach from 132 nm down to 77 nm (**Figure 2b**). Analogous to findings from two- or three-stage co-evaporated absorbers, cross-section scanning electron micrographs suggest improved grain growth and reduction of voids towards the back contact. Despite the detection of C with GD-OES, no residual carbonaceous

layer is apparent between absorber and back contact via scanning electron microscopy (SEM), highlighting the small amount of the impurities (**Figure 2c**). We further compared the GD-OES compositional depth gradients between absorbers from standard and Cu-graded precursor films (**Figure 2d**). Interestingly, we find that absorbers from our standard process exhibit a spontaneous Cu enrichment towards the absorber surface despite the initial homogeneous Cu-distribution in the precursors. We suspect that the comparatively low formation temperatures of Cu-Se phases combined with selenium provision from the surface and the high mobility of liquid phases promote the migration of Cu towards the sample surface.[5, 30] In contrast, the Cu/In ratio throughout the absorber for our Cu-graded samples appears comparatively homogeneous, exhibiting even a low Cu/In ratio towards the absorber surface, which is commonly believed to be beneficial due to the formation of a ordered defect compound (ODC) that aids to reduce interfacial recombination.[31] Similarly, the S/(S+Se) ratio is seen to be more homogeneous for the graded absorber case, removing both high and low sulfur regions in the absorber. Energy dispersive X-ray spectroscopy (EDX) of absorber layers show overall S/(S+Se) ratios around 0.055 while inductively coupled plasma mass spectroscopy (ICP-MS) measurements determine Cu/In ratios around 0.85 (Table S3), the latter being close to ratios reported for highest PCE CIGS devices.[32] X-ray diffraction (XRD) measurements of selenized precursor films further confirm the sulfur incorporation and overall S/(S+Se) ratios in the absorbers (See Fig. S4). Elevated sulfur contents in $CuIn(S,Se)_2$ absorbers lead to an overall increase in the bandgap which is largely administered through a raise in the conduction band. This raise is critical for reducing the conduction band offset towards CdS and enabling efficient charge collection and high fill factor (FF) values under UV-filtered light conditions.[12]
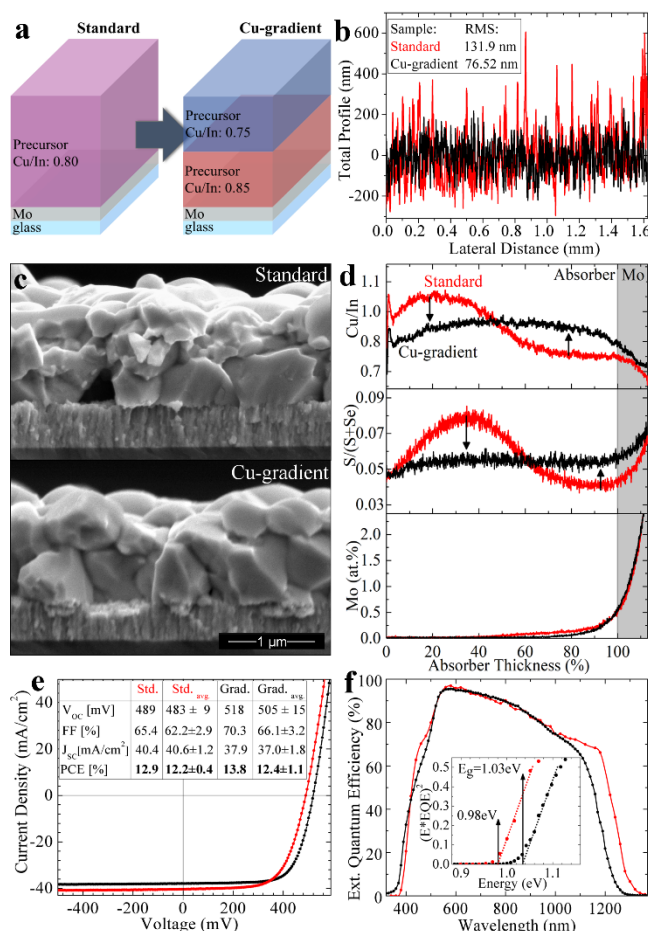
Figure 2 (a) Schematic drawing of Standard and Cu-gradient precursor films. (b) Profilometry data of absorber from Standard and Cu-gradient process indicated reduced RMS roughness with gradient. (c) SEM cross section micrographs showing reduced porosity and improved grain size with Cu-gradient. (d) GD-OES compositional depth profiles in at.% depict more homogeneous Cu/In and S/(S+Se) profiles with the Cu-gradient route. (e) Device champion and average performance data of best 25 cells on a substrate. A record active area PCE of 13.8% could be achieved with the Cu-gradient and DMF solvent. (f) Corresponding EQE(λ) data confirming low minimum bandgaps of 1.0 eV.

Devices were finalized with a CdS buffer layer by chemical bath deposition, ZnO/ITO transparent contact layers by sputtering, Ni/Al grid, and a 110 nm thick MgF_2 antireflection (AR) coating via e-beam evaporation. After mechanical scribing to a cell size around 0.11 cm^2, devices were characterized via current density voltage (J-V) and external quantum efficiency (EQE(λ)) measurements. **Figure 2e** shows a significant improvement in both average and champion active area device efficiencies from 12.2% to 12.4% and 12.9% to

13.8%, respectively, by implementing a Cu-graded precursor route. Improvements are visible in both FF and open-circuit voltage (Voc) while the short circuit current density (Jsc) is slightly decreased. This trend agrees well with corresponding EQE(λ) measurements (**Figure 2f**), where an increase of the minimum absorber bandgap from 0.98 eV to 1.03 eV is detected for devices from standard and graded precursors, respectively, while calculated Jsc values from EQE(λ) decreased from 38.9 mA/cm^2 to 36.4 mA/cm^2. Both GD-OES (Fig. 2d) and XRD data (Fig. S4) suggests that absorbers from the standard precursor route exhibit areas of lower sulfur incorporation, which should contribute to the red shift of the absorption edge as seen by EQE(λ) measurements. Notably, the standard deviation for average performance values showed a slight increase with the adoption of the Cu-gradients. We expect this to be due to the greater finesse of the deposition process which should be overcome with a higher degree of automation. We also tested more pronounced Cu-gradients but obtained lower device PCEs. To further investigate the applicability our molecular-ink route with TU-stabilized Cu(I)Cl, we fabricated CIS devices from inks with other polar solvents or solvent mixtures such as methanol (MeOH) and H$_2$O/DMSO and replaced our commonly inert anneal conditions with annealing ambient air. Table S4 provides a summary of the best obtained device efficiencies under various solvent and anneal conditions with the commonality of high TU/Me ratios of 3, mixing sequence of solvent-TU-CuCl-InCl$_3$, and annealing temperatures of 250°C. Notably, devices from MeOH or H$_2$O-containing inks that were annealed at ambient air exhibited device efficiencies over 10% without AR-coating, exemplifying the robustness and low cost-potential of our method.
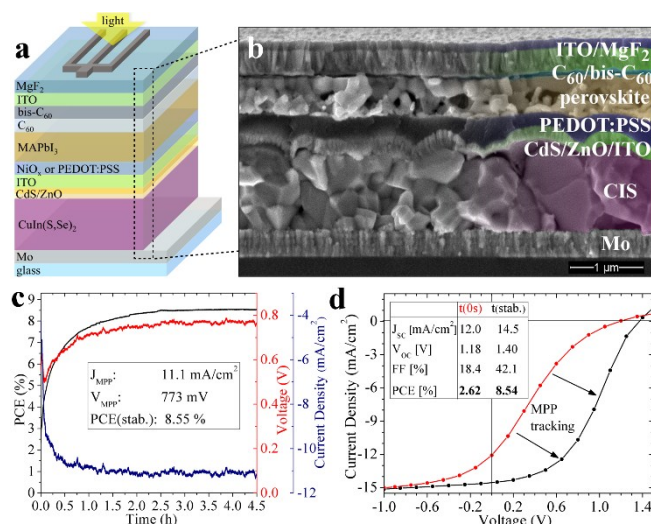
Figure. 3: (a) Schematic of monolithic HP-CIS tandem solar cell. (b) SEM cross-section of tandem solar cell. (c-d) Maximum power point tracking shows improving and stabilizing active area PCE from initial 2.6% up to 8.6% after 4 hours.

To demonstrate the suitability of our solution-processed low-bandgap CIS devices as bottom cells in tandem applications we fabricated monolithic tandem devices with solution-processed perovskite top cells. Similar to previously described, perovskite devices were manufactured in an inverted ITO/HTL/MAPbI$_3$/C$_{60}$/bis-C$_{60}$/cathode architecture with PEDOT:PSS or NiO$_x$ as hole transport layer (HTL).[12] While we could effectively reduce the absorber roughness of our CIS bottom devices by employing a Cu-graded precursor approach (see Figure 2b), the increased roughness as compared to glass (2-5 nm) is still a challenge for the PSC due to the inherent thin film nature of the involved functional layers. To further reduce the likelihood of shunt paths in the PSC top cell via accidental anode and cathode contact, the perovskite absorber thickness was increased from 180-220 nm to 550-600 nm and the C$_{60}$ electron transport layer (ETL) was thermally evaporated rather than spin-coated to ensure conformal coverage.

Low temperature-processing of the top cell is indispensable as CIGS devices have been reported to undergo rapid degradation above 320 °C due to counter doping of the absorber by

cation diffusion from the buffer layer.[33] PEDOT:PSS and NiO_x were therefore selected as HTL for their low-temperature processability at 100°C (see ESI for experimental description). NiO_x based HTLs have been reported to increase Voc and PCE due to better interfacial charge dynamics.[34] Accordingly, we found that opaque single junction PSC on glass with Ag cathodes exhibited significantly improved device performance with NiO_x as compared to PEDOT:PSS – from 11.7% to 17.1% PCE with all device parameters improved (see Figure S5). Analogous semitransparent devices were prepared substituting the Ag cathode with a 300 nm thick layer of sputtered ITO. The devices were directly deposited on the ITO top layer of a CIS solar cell as depicted in **Figure 3a**. For efficient recombination of charge carriers in this ITO layer, the thickness of the latter was reduced to 100 nm corresponding to a sheet resistance of 140 Ohm/sq. Since no lateral transport of carriers is required in the recombination layer, high resistances are tolerable. The SEM cross section micrograph in **Figure 3b** reveals the full tandem architecture and employed layer thicknesses. No shunt paths in the top cell are apparent despite the residual inherent roughness of the CIS bottom cell. The thick PEDOT:PSS layer is seen to effectively fill the crevasses of the bottom cell and create a flat surface for the HP absorber. In contrast, the employed thin NiO_x HTL hardly contributed to a surface smoothening and therefore left a higher risk for shunts in the top cell (see Figure S6). Similar to single junction CIS devices, monolithic tandems were finalized with a 110 nm thick MgF_2 AR-coating and Ni/Al grids via e-beam and thermal evaporation, respectively, before being mechanically scribed to a cell area of 0.11 cm^2. Current-voltage characterization under ambient air conditions revealed a strong light-soaking behavior for tandems with both HTLs. **Figure 3c** shows the improving device parameters during maximum power point (MPP) tracking under simulated AM1.5G light for a PEDOT:PSS-based tandem device. Device performance was seen to stabilize at up to 8.55%

after 4.5 hours. Devices with NiO_x HTLs showed similar light-soaking behavior with stabilized PCEs up to 8.42% (see Figure S7). A comparison of the initial and stabilized J-V curve reveals key improvements through increasing FF with MPP tracking (FF_0=18.4%, FF_{stab}=42.1%, see **Figure 3d**). Stabilized tandem Vocs of up to 1.40 V are close to the added voltages of the individual cells (i.e. CIS: 518 mV, PSC(PEDOT:PSS): 975 mV, sum: 1.49 V) which suggests a good monolithic contact between top and bottom cells and low leakage currents. Notably, we were able to relate the source for our poor FF to our semitransparent perovskite top cells. While high FF and PCEs were obtained in standard superstrate configuration, PSCs exhibited poor FF values and roll-over behavior similar to our tandem cells when measured in substrate configuration (see Figure S8). We suggest that charge carrier extraction to the HTL through the thick HP (550-600 nm) is dramatically reduced in substrate configuration when excitons are mostly generated close to the ETL. The uncollected charge build-up could lead to a potential barrier which presents itself in form of a low FF. Poor morphologies of HP layers, as seen in Fig 3b, that are likely caused by use of rough CIS substrates might further exacerbate this issue. Further improvements in carrier diffusion lengths in the HP via defect passivation or morphology improvements or the use of thinner HP absorbers might remedy this problem and further increase tandem PCEs.

In conclusion, we presented a novel molecular ink route for CIS absorber layers based on DMF, metal chlorides, and TU that allowed for a 10-fold increase in metal concentration as compared to commonly used DMSO inks. This consequently improved ink stability at room temperature and reduced necessary ink deposition and annealing cycles to build absorber thickness. Characterization of the precursor inks suggested that in this route both DMF and TU likely compete in the first coordination shell of dissolved $InCl_3$ while Cu(I) is likely stabilized by TU in a $Cu(TU)_xCl$ complex, as previously shown by Uhl et al.[17] The latter

complex is thought to be crucial to stabilize copper in oxidation state +1 and omit the necessity for additional redox reaction in order to form the I-III-IV$_2$ absorber that is CIS. The robustness and applicability of this ink chemistry is exemplified by extending the molecular ink route to MeOH and H$_2$O-based solvents which yield devices with over 10% PCE without AR-coating, even when precursors are annealed in ambient air. Using GD-OES depth profiling, we compared the residual carbon content in devices employing our DMF-based, solution-processed CIS absorbers with devices with co-evaporated CIS absorbers and found similar carbon profiles with main carbon accumulation between the absorber and the Mo back contact for both samples. This suggests that the amount of residual carbon of solution-processed absorbers is comparable to the carbon amount induced through sample exposure with ambient air (i.e. by transfer between vacuum chambers) and might not be detrimental to device performance (see also [4, 35]). Cu-graded precursors were presented as means to control the surface roughness, Cu/In and S/(S+Se) ratios of the absorber, and increase device PCE. By employing Cu-graded precursors and DMF-based molecular inks with TU, the champion active area efficiency for CIS devices could be increased up to 13.8% (Newport certified: 13.1%, see Table S5), which is a new world record for solution-processed CIS devices and solution-processed solar cells with a bandgap at 1.0 eV.

CIS devices were further employed as bottom cells in solution-processed monolithic tandem devices with perovskite top cells. Stabilized PCEs up to 8.55% were obtained with Vocs up to 1.40 V which resembles near perfect voltage addition between top and bottom cells. Tandem PCEs were found to be limited mainly by low FF values which were seen to dramatically improve with light soaking under MPP. This problem was related to the performance of our semitransparent PSCs which suffered from poor morphologies when deposited on CIS substrates and experienced dramatic FF losses when operated in substrate

configuration with illumination through the ETL, suggesting a carrier extraction problem in the top cell. Increased tandem PCEs can therefore be expected from tandem devices with thinner HP absorbers and improved carrier diffusion length and morphology. Collectively, these results highlight the potential of solution-processing methods for high efficiency thin film single junction and monolithic tandem solar cells based on CIS and HP absorbers as means to dramatically reduce the cost of clean and renewable electricity from the sun.

Supporting Information

Supporting Information is available from the Wiley Online Library or from the author.

Acknowledgements

References

[1]   IPCC, **2014**: Climate Change 2014: Synthesis Report. Contribution of Working Groups I, II and III to the Fifth Assessment Report of the Intergovernmental Panel on Climate Change [Core Writing Team, R.K. Pachauri and L.A. Meyer (eds.)]. IPCC, Geneva, Switzerland, 151 pp.

[2]   P. Jackson, R. Wuerz, D. Hariskos, E. Lotter, W. Witte, M. Powalla, Phys. Status Solidi RRL **2016**, 10, 583; W. S. Yang, B.-W. Park, E. H. Jung, N. J. Jeon, Y. C. Kim, D. U. Lee, S. S. Shin, J. Seo, E. K. Kim, J. H. Noh, S. I. Seok, Science **2017**, 356, 1376; A. Green Martin, Y. Hishikawa, D. Dunlop Ewan, H. Levi Dean, J. Hohl-Ebinger, W. Y. Ho-Baillie Anita, Progress in Photovoltaics: Research and Applications **2017**, 26, 3.

[3]   M. Saliba, T. Matsui, K. Domanski, J.-Y. Seo, A. Ummadisingu, S. M. Zakeeruddin, J.-P. Correa-Baena, W. R. Tress, A. Abate, A. Hagfeldt, M. Grätzel, Science **2016**, 354, 206.

[4]   A. R. Uhl, C. Fella, A. Chirilă, M. R. Kaelin, L. Karvonen, A. Weidenkaff, C. N. Borca, D. Grolimund, Y. E. Romanyuk, A. N. Tiwari, Prog. Photovolt. **2012**, 20, 526.

[5]   A. R. Uhl, P. Fuchs, A. Rieger, F. Pianezzi, C. M. Sutter-Fella, L. Kranz, D. Keller, H. Hagendorfer, Y. E. Romanyuk, F. LaMattina, S. Yoon, L. Karvonen, T. Magorian-Friedlmeier, E. Ahlswede, D. VanGenechten, F. Stassin, A. N. Tiwari, Prog. Photovolt. **2015**, 23, 1110.

[6]   A. De Vos, J. Phys. D: Appl. Phys. **1980**, 13, 839; R. F. Service, Science **2014**, 344, 458; M. A. Green, A. Ho-Baillie, H. J. Snaith, Nature Photonics **2014**, 8, 506; Z. M. Beiley, M. D. McGehee, Energy Environ. Sci. **2012**, 5, 9173.

[7]   M. A. Green, Y. Hishikawa, W. Warta, E. D. Dunlop, D. H. Levi, J. Hohl-Ebinger, A. W. H. Ho-Baillie, Progress in Photovoltaics: Research and Applications **2017**, 25, 668.

[8]   O. Ergen, T. Pham, A. Zettl, Nature Materials **2016**, doi:10.1038/nmat4795; A. Kojima, K. Teshima, Y. Shirai, T. Miyasaka, J. Am. Chem. Soc. **2009**, 131, 6050.

[9]   S. D. Wolf, J. Holovsky, S.-J. Moon, P. Löper, B. Niesen, M. Ledinsky, F.-J. Haug, J.-H. Yum, C. Ballif, J. Phys. Chem. Lett. **2014**, 5, 1035; S. Albrecht, B. Rech, Nature Energy **2017**, 2, 16196.

[10]   S. Yun, Y. Qin, A. R. Uhl, N. Vlachopoulos, M. Yin, D. Li, X. Han, A. Hagfeldt, Energy & Environmental Science **2018**, DOI:10.1039/C7EE03165C; T. Duong, Y. Wu, H. Shen, J. Peng, X. Fu, D. Jacobs, E. C. Wang, C. Kho Teng, C. Fong Kean, M. Stocks, E. Franklin, A. Blakers, N. Zin, K. McIntosh, W. Li, Y. B. Cheng, P. White Thomas, K. Weber, K. Catchpole, Advanced Energy Materials **2017**, 7, 1700228; H. Shen, T. Duong, J. Peng, D. Jacobs, N. Wu, J. Gong, Y. Wu, S. K. Karuturi, X. Fu, K. Weber, X. Xiao, T. P. White, K. Catchpole, Energy & Environmental Science **2018**, 11, 394; D. Zhao, C. Wang, Z. Song, Y. Yu, C. Chen, X. Zhao, K. Zhu, Y. Yan, ACS Energy Letters **2018**, 3, 305.

[11]   A. Chirilă, S. Buecheler, F. Pianezzi, P. Bloesch, C. Gretener, A. R. Uhl, C. Fella, L. Kranz, J. Perrenoud, S. Seyrling, R. Verma, S. Nishiwaki, Y. E. Romanyuk, G. Bilger, A. N. Tiwari, Nature Materials **2011**, 10, 857.

[12]   A. R. Uhl, Z. Yang, A. K.-Y. Jen, H. W. Hillhouse, J. Mater. Chem. A **2017**, 5, 3214.

[13]   F. Meillaud, A. Shah, C. Droz, E. Vallat-Sauvain, C. Miazza, Sol. Energ. Mat. Sol. C. **2006**, 90, 2952.

[14]   I. L. Braly, R. J. Stoddard, A. Rajagopal, A. R. Uhl, J. K. Katahara, A. K. Y. Jen, H. W. Hillhouse, ACS Energy Letters **2017**, 2, 1841; K. A. Bush, A. F. Palmstrom, Z. J. Yu, M. Boccard, R. Cheacharoen, J. P. Mailoa, D. P. McMeekin, R. L. Z. Hoye, C. D. Bailie, T. Leijtens, I. M. Peters, M. C. Minichetti, N. Rolston, R. Prasanna, S. Sofia, D. Harwood, W. Ma, F. Moghadam, H. J. Snaith, T. Buonassisi, Z. C. Holman, S. F. Bent, M. D. McGehee, Nature Energy **2017**, 2, 17009; A. Rajagopal, Z. Yang, S. B. Jo, I. L. Braly, P.-W. Liang, H. W. Hillhouse, A. K. Y. Jen, Advanced Materials **2017**, 1702140.

[15]   T. Todorov, T. Gershon, O. Gunawan, Y. S. Lee, C. Sturdevant, L. Y. Chang, S. Guha, Adv. Energy Mater. **2015**, 5, 1500799.

[16]   Y. H. Jang, J. M. Lee, J. W. Seo, I. Kim, D.-K. Lee, Journal of Materials Chemistry A **2017**, 5, 19439.

[17]   A. R. Uhl, J. K. Katahara, H. W. Hillhouse, Energy & Environmental Science **2016**, 9, 130.

[18]   A. D. Collord, H. W. Hillhouse, Chemistry of Materials **2016**, 28, 2067.

[19]   D. Tiwari, T. Koehler, X. Lin, A. Sarua, R. Harniman, L. Wang, R. Klenk, D. J. Fermin, ACS Applied Materials & Interfaces **2017**, 9, 2301.

[20]   D. M. Adams, A. J. Carty, P. Carty, D. G. Tuck, J. Chem. Soc. A **1968**, 162.

[21]   K. Otto, P. Bombicz, J. Madarász, I. Oja Acik, M. Krunks, G. Pokol, Journal of Thermal Analysis and Calorimetry **2011**, 105, 83.

[22]   V. Venkata Chalapathi, K. Venkata Ramiah, Proceedings of the Indian Academy of Sciences - Section A **1968**, 68, 109; T. Ishiguro, E.-i. Suzuki, A. Y. Hirakawa, M. Tsuboi, J. Mol. Spectrosc. **1980**, 83, 360.

[23]   T. Cottineau, M. Richard-Plouet, J.-Y. Mevellec, L. Brohan, The Journal of Physical Chemistry C **2011**, 115, 12269.

[24]   S.-i. Ishiguro, K. Ozutsumi, H. Ohtaki, Bulletin of the Chemical Society of Japan **1987**, 60, 531; K. Ishihara, S. Funahashi, M. Tanaka, Inorg. Chem. **2002**, 25, 2898.

[25]   D. R. Lide, *CRC Handbook of Chemistry and Physics, 84th Edition*, CRC Press, Boca Raton, FL, USA **2003**.

[26]   S. Wang, Q. Gao, J. Wang, J. Phys. Chem. B **2005**, 109, 17281.

[27]   J. A. Clark, A. R. Uhl, T. R. Martin, H. W. Hillhouse, Chemistry of Materials **2017**, 29, 9328.

[28]   T. Feurer, B. Bissig, T. P. Weiss, R. Carron, E. Avancini, J. Löckinger, S. Buecheler, A. N. Tiwari, Science and Technology of Advanced Materials **2018**, 19, 263.

[29]   D. Rudmann, Vol. Ph.D., ETH Zurich, **2004**; I. Repins, M. A. Contreras, B. Egaas, C. DeHart, J. Scharf, C. L. Perkins, B. To, R. Noufi, Progress in Photovoltaics: Research and Applications **2008**, 16, 235.

[30]   A. R. Uhl, M. Koller, A. S. Wallerand, C. M. Fella, L. Kranz, H. Hagendorfer, Y. E. Romanyuk, A. N. Tiwari, S. Yoon, A. Weidenkaff, T. M. Friedlmeier, E. Ahlswede, D. VanGenechten, F. Stassin, Thin Solid Films **2013**, 535, 138.

[31]   T. Minemoto, T. Matsui, H. Takakura, Y. Hamakawa, T. Negami, Y. Hashimoto, T. Uenoyama, M. Kitagawa, Solar Energy Materials and Solar Cells **2001**, 67, 83; W. Witte, R. Kniese, M. Powalla, Thin Solid Films **2008**, 517, 867.

[32]   P. Jackson, D. Hariskos, R. Wuerz, O. Kiowski, A. Bauer, T. Magorian-Friedlmeier, M. Powalla, physica status solidi (RRL) - Rapid Research Letters **2016**, 9, 28.

[33]   S. Kijima, T. Nakada, Appl. Phys. Express **2008**, 1, 075002.

[34]   J. H. Kim, P.-W. Liang, S. T. Williams, C. Cho Namchul, Chu-Chen, M. S. Glaz, D. S. Ginger, A. K. J. Jen, Advanced Materials **2015**, 27, 695; J. W. Jung, C.-C. Chueh, A. K.-Y. Jen, Advanced Materials **2015**, 27, 7874.

[35]   V. Haug, A. Quintilla, I. Klugius, E. Ahlswede, Thin Solid Films **2011**, 519, 7464.

The table of contents entry

Alexander R. Uhl*, Adharsh Rajagopal, James A. Clark, Anna Murray, Thomas Feurer, Stephan Buecheler, Alex K.-Y. Jen, Hugh W. Hillhouse*

Solution-processed low-bandgap CuIn(S,Se)$_2$ absorbers for high efficiency single junction and monolithic chalcopyrite-perovskite tandem solar cells
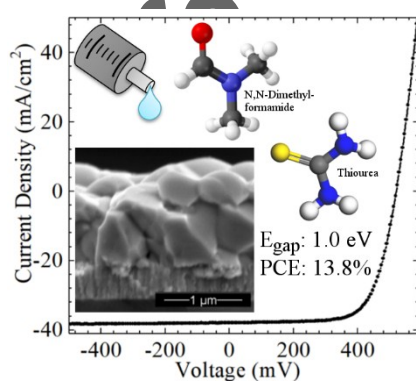
Thin film CuIn(S,Se)$_2$ solar cells with high efficiencies up to 13.8% are presented using absorbers from a molecular-ink route based on off-the-shelf chemicals N,N-dimethylformamide, thiourea, and metal chlorides. The former greatly improved ink stability while compositionally-graded precursors reduced absorber roughness to enable monolithic tandem devices with perovskite top cells yielding near perfect voltage addition up to 1.40 V.